Modeling of Interstellar Scintillation Arcs from Pulsar B1133+16

Frank S. Trang [1]
Department of Electrical & Computer Engineering
University of California San Diego La Jolla, CA 92093-0407
and Avaak, Inc., 5405 Morehouse Dr., San Diego, CA 92121

Barney J. Rickett [2]
Department of Electrical & Computer Engineering
University of California San Diego La Jolla, CA 92093-0407

ABSTRACT

The parabolic arc phenomenon visible in the Fourier analysis of the scintillation spectra of pulsars provides a new method of investigating the small scale structure in the ionized interstellar medium (ISM). We report archival observations of the pulsar B1133+16 showing both forward and reverse parabolic arcs sampled over 14 months. These features can be understood as the mutual interference between an assembly of discrete features in the scattered brightness distribution. By model-fitting to the observed arcs at one epoch we obtain a "snap-shot" estimate of the scattered brightness, which we show to be highly anisotropic (axial ratio $> 10:1$), to be centered significantly off axis and to have a small number of discrete maxima, which are coarser the speckle expected from a Kolmogorov spectrum of interstellar plasma density. The results suggest the effects of highly localized discrete scattering regions which subtend 0.1-1 mas, but can scatter (or refract) the radiation by angles that are five or more times larger.

Subject headings: ISM: general — scattering — plasmas — pulsars: individual (B1133+16)

1. Introduction

The scattering of the radio waves as they propagate through the ISM has long been a clue to small scale inhomogeneities in the ionized interstellar plasma. The scattering is seen in the dynamic spectrum of pulsar signals as random modulations in frequency and time. Islands of intensity in the dynamic spectrum, often referred to as "scintles", are sometimes modulated by a criss-cross pattern. By Fourier analyzing the dynamic spectrum, Stinebring et al. (2001) discovered the remarkable phenomenon of parabolic arcs that underlies the criss-cross substructure. In this paper, we analyze parabolic arcs from archival observations of PSR B1133+16 originally reported by Gupta, Rickett, & Lyne (1994).

The two-dimensional Fourier spectrum of the primary dynamic spectrum is often referred to as the secondary spectrum. However, as described by Cordes et al. (2006), it can also be regarded as the "differential delay-Doppler" distribution, whose coordinates are time delay (f_ν) and Doppler frequency (or fringe rate f_t), being the variables conjugate to radio frequency ν and time t. The theory of the arcs is described in that paper, which henceforth we refer to as CRSC, and is also discussed by Walker at al. (2004).

The basic arc phenomenon is remarkably simple, even though it lay undiscovered for over 30 years. When scattered waves arrive at the observer from two angles they interfere and cause fringes in intensity. The observer is moving relative to this interference pattern and sees a sinu-

[1]e-mail:iknowfrank@yahoo.com
[2]e-mail: bjrickett@ucsd.edu

soidal variation in both time and frequency, which thus appears as a pair of points in the secondary spectrum. The coordinates of these points are the differences in group delay and Doppler frequency between the two scattered waves. The Doppler shift depends on the relative velocity between the source and observer along the (scattered) lines of sight. Hence the *difference* in Doppler shift of waves scattered along two different paths through the ISM depends only on the angles of scattering and the *transverse* velocity of the observer and pulsar relative to the ISM. It is the beating of these slightly different Doppler shifts that makes the fringe vary in time and so their difference equals the fringe rate f_t. There is a quadratic relation of delay to fringe rate because, while the delay depends on the square of the angle of scattering, the Doppler shift depends linearly on the angles. When one of the waves is unscattered the result is a simple parabola $f_\nu \propto f_t^2$.

The observational properties of pulsar scintillation arcs have been described by Hill et al. (2003), who observed arcs over a broad range of wavelengths and found the curvature to be remarkably constant and to follow the expected scaling as wavelength squared. Arc observations from five pulsars are shown by CRSC, who summarize the various arc phenomenon. The results show many deviations from the simple arc $f_\nu \propto f_t^2$. A particuarly striking form is the occasional appearance of "reverse arclets" which are displaced from the origin and whose curvature is equal in magnitude, but reversed in sign, to that of the main (forward) arc. Hill et al. (2005) reported on a set of remarkable stable reverse arclets from PSR B0834+06.

We present results for the evolution of the arcs seen in PSR B1133+16 at 408 MHz in archival observations spanning 16 months. On two of the days observed with short time resolution the delay-Doppler spectrum showed several discrete arcs with reversed curvature, similar to those shown by Hill et al. (2005). We concentrate on fitting a model to one of those days. From an assumed brightness distribution we calculate the expected delay-Doppler spectrum using the screen theory of CRSC. Then we iteratively adjust the parameters of the model to fit to the observed spectrum. Although the fitting is not unique we are able to explain the reversed arcs and obtain an estimate of the scattered brightness distribution. This model distribution is then compared with that expected from a Kolmogorov scattering medium. We finish with a brief discussion of what structures in the interstellar medium might be responsible.

The technique we use, which is model-fitting to match the observed secondary spectrum, differs from the inversion described by Walker and Stinebring (2005), who perform the match to the primary dynamic spectrum. We discuss the differences between the two methods in §3.1.

2. Observations and Data Analysis

The observations were made with the 76m telescope at Jodrell Bank between September 1984 and January 1986, as described by Gupta, Rickett, & Lyne (1994). An auto-correlation spectrometer was centered at 408 MHz with 256 channels of 20 kHz covering 5 MHz. The spectrometer was gated synchronously with the pulsar period and spectra were averaged in windows on and off the pulse. The averaging time was normally 30 seconds and on two occasions it was shortened to 10 seconds. The duration ($T_{\rm obs}$) of most observations was from one to four hours. The on and off pulse spectra were corrected for the one-bit auto-correlation normalized and subtracted to create a primary dynamic spectrum of pulse intensity $S(\nu, t)$.

The left hand panels of Figure 1 shows $S(\nu, t)$ for 8 and 9 September 1984 (which we call days 0 and 1 of the observing sequence); they exhibit crisscross structure with a predominance of scintles that drift toward higher frequency with time. With the 10 second sampling one can see fine scale fringes drifting in the same direction.

The right panels are the corresponding secondary spectrum – $S_2(f_\nu, f_t)$ or delay-Doppler spectrum, which is the squared magnitude of the Fourier Transform of the primary spectrum:

$$S(\nu, t) \quad \longrightarrow \quad S^\dagger(f_\nu, f_t) \tag{1}$$

$$S_2(f_\nu, f_t) \quad = \quad |S^\dagger(f_\nu, f_t)|^2 \, . \tag{2}$$

Here $S^\dagger(f_\nu, f_t)$ is the two dimensional discrete Fourier transform of the sampled primary spectrum $S(\nu, t)$. With time resolution of 10 seconds and frequency resolution of 20kHz, the Nyquist frequencies are $f_{t,\rm Nyq} = 3$ cycles min^{-1} (cpm) and $f_{\nu,\rm Nyq} = 25.6$ cycles/MHz (or 25.6 μsec). The as-

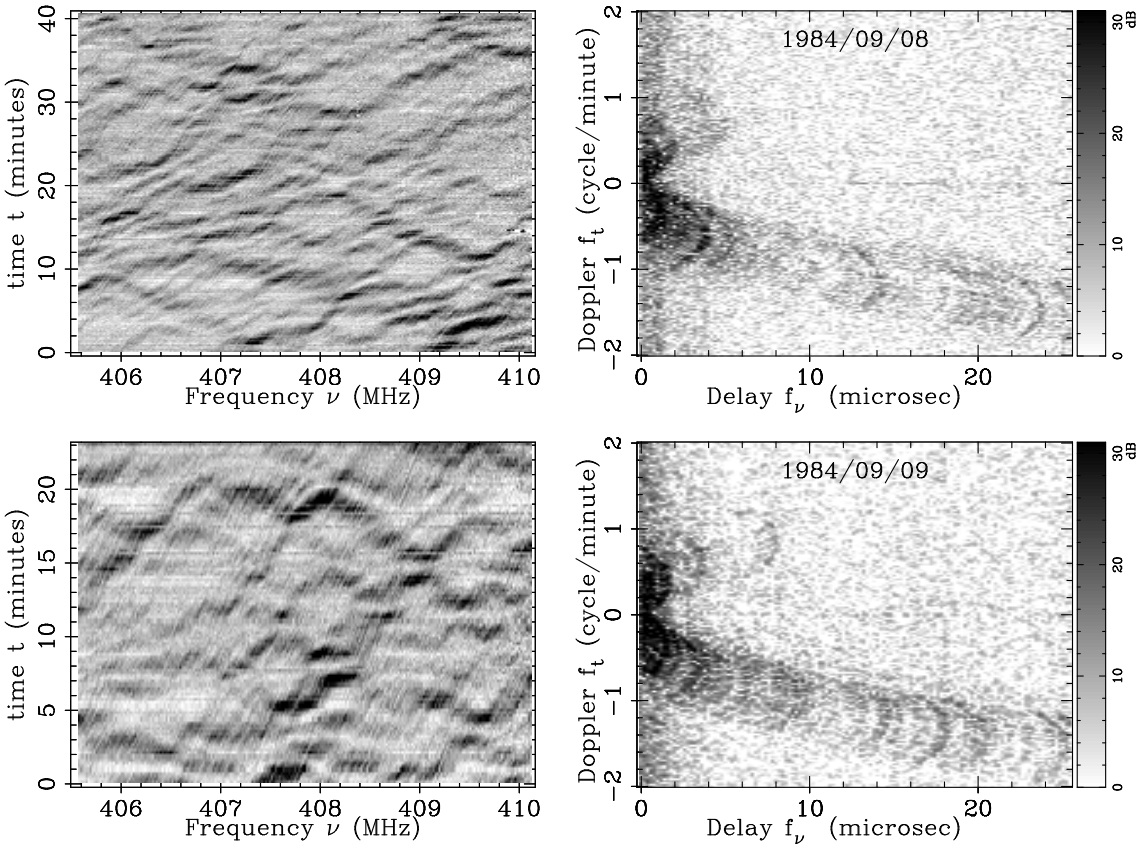

Fig. 1.— *Top Left:* Dynamic Spectrum of PSR B1133+16 on 8th September 1984 (day 0) with sampling time of 10 seconds. *Top Right:* Secondary Spectrum of the same data. The plot is limited to ±2 cpm in f_t, since no signal is visible in the range 2-3 cpm. The grey scale is logarithmic from the mean noise level to black at a level 30dB higher, as shown by the tablet to the right. The plot shows a set of reversed arcs grouped together forming a forward parabolic arc predominantly visible for negative f_t. *Bottom Left and Right:* Same displays for 9th September 1984. Note that the different time scale from that above; both show narrow fringes that drift in the same general sense. Both secondary spectra are similar, but the details of the reverse arcs have changed over one day.

sociated spectral resolutions are $\delta f_t = 1/T_{\rm obs}$ and $\delta f_\nu = 0.2\mu$sec.

The S_2 plots show structure which is strongest near the origin and extends out to large delays (f_ν) in the lower part of the panel (ie for negative f_t). We call this the forward arc, since it is curved toward the f_ν axis. It consists of discrete curves, which we call reverse arcs, since they are curved in the opposite sense. The apexes of the reverse arcs lie approximately along the parabola $f_\nu \propto f_t^2$. On close inspection one can see several nearly parallel forward arcs. The top and bottom panels of Figure 1 are separated by 27 hrs and show very similar behavior in general, but the individual reverse arcs have clearly changed substantially. The main goal of our paper is to investigate these reverse arcs and to find a model for the interstellar angular scattering function that could explain them.

2.1. Time Evolution of the Arcs

After rapidly sampled observations were made on September 8th and 9th 1984, a slower standard sampling interval of 30 seconds was adopted for monitoring the ISS of PSR B1133+16. Figure 2 shows S_2 plots from twelve observations spanning 481 days. Days 0-31 show the same general

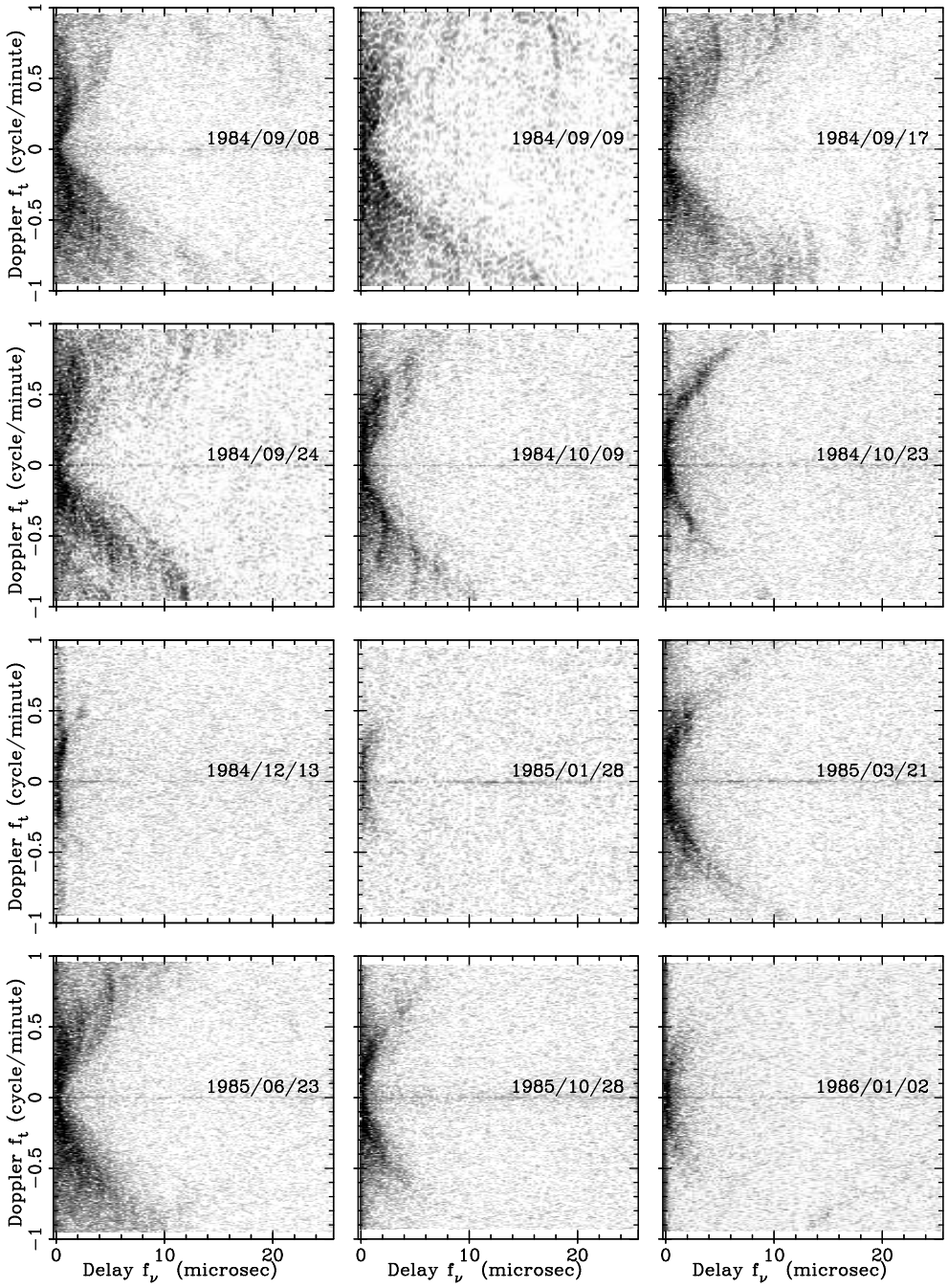

Fig. 2.— Selected Secondary Spectra of PSR B1133+16 from September 1984 to January 1986 in a logarithmic grey scale over a 30 dB dynamic range, as shown by the tablet in Figure 1

character of a V-shaped "valley" with little power along the delay axis, flanked by diffuse power often appearing as a set of discrete reverse arcs, which can be asymmetric in f_t. Then day 45 shows a simpler forward arc which fades remarkably over days 96 and 142. A strong forward arc appears on day 194 and by day 288 multiple reverse arcs similar to days 0-31 have returned. Day 415 is similar to day 194, but day 481 has weak and indistinct arc structure. These remarkable changes in the appearance of the secondary spectra are evidence that the line of sight crossed through particular localized structures, as we discuss in § 4.

With 30 second sampling $f_{t,\mathrm{Nyq}} = 1$ cpm, and so features beyond ± 1 cpm can be aliassed into the figure. This is evident by comparing the plots for days 0 and 1 in figures (2) and (1). For example on day 1 figure (2) shows a linear feature at $f_t \sim 0.75 \pm 0.15$ cpm and $f_\nu \sim 18\mu$sec. This is an alias from $f_t \sim 0.75 - 2.0 = -1.25$ cpm, visible in the lower right panel of Figure 1 at $f_\nu \sim 18\mu$sec with its apex near $f_t = -1.4$ cpm. The figure (1) data were a 23 minute observation immediately following the 30 min observation figure (2). This discrete reverse arc changed very little in 40 minutes. Though it clearly changed between day 0 and 1. Days 9 and 16 show fuzzy reverse arcs for both positive and negative f_t, which are probably confused by aliasing, but give evidence for an evolution in the asymmetry as well as in the reverse arc features.

In one of the observations of PSR B1133+16 shown by CRSC the secondary spectrum has two very well defined discrete forward arcs. Putney and Stinebring (2006) have found multiple arcs in six pulsars. For B1133+16 they found the arc curvatures to fall near four discrete values, but that the arc strengths were quite variable. They suggest that these are due to variable amplitude scattering at four discrete distances from the Earth. Consequently, we have estimated the curvature a (defined by $f_\nu = a f_t^2$) from each of our observations scaled to 1 GHz. The mean of our values over 1984 September to 1986 January was $a = 6.7 \times 10^{-3}$ sec^3 with an rms scatter of 0.6×10^{-3} sec^3 , which is consistent with one of their values at $(6.3 \pm 0.1) \times 10^{-3}$ sec^3. We do not detect multiple forward arcs, but note the signal-to-noise ratio in our data is lower than in most of Stinebring's data. We also note that the curvature estimation becomes more difficult in the presence of reverse arclets, and in such cases we trace the arc by the location of their apexes.

3. Modeling of arcs from PSR B1133+16

3.1. Theory

We use the theory of arcs in the secondary spectrum as given by CRSC. Section 3.3 of that paper analyzes S_2 in terms of a "brightness function" $B(\theta_x, \theta_y)$ that represents the instantaneous strength of contributions to the intensity at a given observing point as a function of the angle of arrival $\boldsymbol{\theta} = (\theta_x, \theta_y)$. The theory provides insight into the basic interference effects that give rise to the arc phenomenon, but it does not include the dispersive delays introduced by propagation through the irregular plasma density in the ISM. In §3.5 we use a full electromagnetic simulation to include such effects.

Consider a pulsar at distance D whose radiation is scattered by a screen at a distance sD from the pulsar. The observer sees a superposition of interference fringes from each pair of apparent angles of arrival $\boldsymbol{\theta}_1$ and $\boldsymbol{\theta}_2$. The fringes contribute to a single pixel in $S_2(f_\nu, f_t)$ if the angles obey:

$$f_\nu = \left(\frac{D(1-s)}{2\,c\,s}\right)\left(\theta_2^2 - \theta_1^2\right) \qquad (3)$$

$$f_t = \left(\frac{1}{\lambda\, s}\right)(\theta_{x2} - \theta_{x1}) V_{\mathrm{iss}}, \qquad (4)$$

where c is the speed of light and λ is the central wavelength observed. $\mathbf{V}_{\mathrm{iss}}$ is the effective transverse velocity relative to the scattering region of the line of sight from pulsar to observer, which both may be moving (Cordes and Rickett, 1998); without loss of generality we have chosen the orientation of $\mathbf{V}_{\mathrm{iss}}$ to define the direction of θ_x.

Equation (8) of CRSC expresses $S_2(f_\nu, f_t)$ as a four-fold integral over all pairs of angles, subject to the constraints of equations 3 and 4. The constraints allow the result to be reduced to a two-fold integral as given by CRSC equations (9) or (B4 & B5). We used the latter, since it is more convenient numerically, and we rewrite it here in a slightly different form as $s_2(q, p)$ which is the delay-Doppler spectrum in terms of normalized de-

lay and fringe rate:

$$p = f_\nu \frac{2cs}{D(1-s){\theta_0}^2}, \qquad q = f_t \frac{s\lambda}{V_{\rm iss}\theta_0} \tag{5}$$

θ_0 is a normalizing angle, typically chosen to be the angular radius of the diffractive brightness distribution.

The result is

$$\begin{aligned} s_2(p,q) &= \frac{\pi}{q}\int_{-\infty}^{\infty}\int_{-\infty}^{\infty} b(\xi_+, y_1)b(\xi_-, y_2)dy_1 dy_2 \\ \xi_\pm &= \frac{p}{2q} \pm \frac{q}{2} - \frac{1}{2q}({y_2}^2 - {y_1}^2) \end{aligned} \tag{6}$$

where $b(x, y)$ is the brightness function in terms of normalized angular coordinates $x = \frac{\theta_x}{\theta_0}, y = \frac{\theta_y}{\theta_0}$, and the constraints in equations (3 & 4) become:

$$\begin{aligned} p &= ({x_2}^2 - {x_1}^2) + ({y_2}^2 - {y_1}^2) \\ q &= x_2 - x_1. \end{aligned} \tag{7}$$

There is also a second mirrored relation obtained by mapping $p \Rightarrow -p, q \Rightarrow -q$.

Hence we can describe an arc as the locus of points in p, q due to interference of a narrow discrete component in $b(x, y)$ at x_p, y_p with the remaining extended continuum in b, as is done in section 3.4.3 of CRSC. A primary forward arc $p \geq q^2$ comes from an undeviated discrete component in b interfering with the extended continuum in b. This is the condition under weak scintillation described by CRSC. The boundary of this primary arc is $f_\nu = a f_t^2$ (or $p = q^2$). In turn a is related to the physical parameters via equations 4 and 3.

In general we substitute x_p, y_p for x_2, y_2 in equation (7) to obtain a relation between p and q depending on x_1 and y_1, which vary over the continuum in b. The special case where b is narrow in one dimension and extended along a line $y_1 = x_1 \tan\phi$, at an angle ϕ to the x-axis, allows us to eliminate both x_1 and y_1 to obtain the quadratic relation between p and q:

$$p = x_p^2 + y_p^2 - \sec^2(\phi)\,(q - x_p)^2. \tag{8}$$

This reverse arc is a parabola with an apex at $p_a = x_p^2 + y_p^2, q_a = x_p$ and negative curvature $-\sec^2(\phi)$, which has unit magnitude if $\phi = 0$ (i.e. scatter broadening parallel to the velocity). The corresponding forward arc with its apex at negative p is obtained by reversing the signs of p and q in equation (8). Both sets of arcs are shown in Figure 4 of CRSC.

Of course, in general the scatter broadening function is not one-dimensional, as assumed above. Further, we have not discussed the power density of s_2 along an arc. This depends on the relative strength of the discrete component supposed to exist in b and on the shape and intensity of its continuum, as described by the integral (6).

3.2. Model for September 8th 1984 (day 0)

The parallax and proper motion of PSR B1133+16 were measured by Brisken et al. (2002); they found its distance $D = 0.35 \pm 0.02$ kpc and its transverse velocity $V_{\rm pm} = 631 \pm 36$ km sec^{-1}. In general the scintillation velocity depends on the transverse velocities of the pulsar, the Earth and the scattering medium, but since our pulsar is moving much faster than the Earth and the medium, we have $V_{\rm iss} = V_{\rm pm}(1-s)$. Hence the arc curvature, as given by equation (8) of Stinebring et al. (2001), becomes:

$$a = \frac{D\lambda^2}{2cV_{\rm pm}^2}\frac{s}{1-s} = 0.0244\frac{s}{1-s}\ \sec^3\,, \tag{9}$$

at our observing wavelength. The arc curvature $a = 6.7 \times 10^{-3}$ sec^3, given in section 2.1, is scaled to 1 GHz. When scaled back to our observed frequency of 408 MHz, we have $a = 0.040 \pm 0.003$ sec^3. This results in $s = 0.62$, giving a screen at 133 ± 7 pc from the Earth. Putting the mean value into equations 3 and 4 gives the mappings:

$$\begin{aligned} f_{t,\rm cpm} &= 0.15\,(\theta_{x2,\rm mas} - \theta_{x1,\rm mas}) \\ f_{\nu,\mu\rm sec} &= 0.26\,(\theta_{2\rm mas}^2 - \theta_{1\rm mas}^2). \end{aligned} \tag{10}$$

The secondary spectrum from September 8th 1984 shown in the upper right panel of Figure 1 exhibits a series of reverse arcs extending to delays of 25 μsec, which are visible predominantly at negative f_t. We choose these data to model quantitatively, because of these unusual *asymmetric discrete reverse* arcs. Consider, for example, the faint reverse arc with its apex at $f_\nu = 14\,\mu$sec and $f_t = -1.1$ cpm, which is visible over the approximate range $-1.6 \leq f_t \leq -0.8$ cpm.

A discrete reverse arc is formed by interference of a point component in the scattered brightness

function with an anisotropic extended component. To simplify the analysis consider the normalized brightness $b(x, y)$ to be narrow in y and extended in x, i.e. parallel to the ISS velocity (i.e. $\phi = 0$ in equation(8)). Thus we write $b(x, y) = [a_p\delta(x - x_p) + b_e(x)]\delta(y)$, where b_e represents the extended component and we use delta functions to model the narrow structures. The interference between waves from x_p and x gives $q = x_p - x$. Thus, if $b_e(x)$ extends from x_- to x_+, the reverse arc will have its apex at $p_a = x_p^2$, $q_a = x_p$ and be visible over $x_- - x_p \leq q \leq x_+ - x_p$.

In this model $y = 0$ and the apex lies on the basic arc. Hence substituting f_ν and f_t from above into equation (9) gives $s = 0.63$, which is consistent with the value 0.63 obtained above. Using the mapping in equation 10, the observed range $-1.6 \leq f_t \leq -0.8$ cpm for the reverse arc, corresponds to interference of a discrete component at -7.5 mas interfering with an extended component from -2.7 mas to 2.7 mas. In a similar way for each discrete reverse arc on day 0 we can find a corresponding pair of components in the scattered brightness (a point and extended component along θ_x).

Following this idea we model the brightness distribution (in normalized coordinates) as a sum of Gaussian functions:

$$b(x, y) = \sum_{i=1}^{n} A_i e^{-\left(\frac{x-x_{oi}}{\sigma_{xi}}\right)^2 - \left(\frac{y-y_{oi}}{\sigma_{yi}}\right)^2} \qquad (11)$$

where A_i is the intensity, σ_{xi} describes the width of x, σ_{yi} describes the width of y, x_{oi} is the offset in x, and y_{oi} is the offset in y. We made an initial model in the manner described above for the most obvious reverse arcs in Figure 1. As more components are added the extended component eventually becomes the sum of the discrete components. Then we tried to optimize the model by minimizing the sum of the squared errors between the observed s_2 and the model obtained by a numerical integral of equation (6).

3.3. Fitting Process

We chose to work in normalized delay p, fringe rate q and angle x, y and used a normalizing angle $\theta_0 = 3.1$ mas, with the constants evaluated as discussed above. The fitting was done over two regions where the arcs are visible in the top right panel of Figure 1: a lower rectangle -2–0 cpm by 0–25 μs and a smaller upper rectangle 0–1 cpm by 0–5 μs.

We estimated the noise background in S_2 from the average noise level in S_2 over the regions not included in the fit, and this constant was added to the model. We defined χ^2 in a standard fashion:

$$\chi^2 = \sum^{i,j} \frac{[S_2(f_{\nu,i}, f_{t,j}) - S_{2,\mathrm{mod},i,j}]^2}{\sigma_{i,j}^2}, \qquad (12)$$

where $\sigma_{i,j} = S_{2,\mathrm{mod},i,j}$. At each point $S_2(f_{\nu,i}, f_{t,j})$ is an estimate of the secondary spectrum, which has a standard deviation $\sigma_{i,j}$ equal to its mean value (following exponential statistics). Once the model is close to an optimum value it provides an estimate of $\sigma_{i,j}$. Thus we used the model as an estimate for $\sigma_{i,j}$ rather than the observed value.

The fitting was done in a semi-automated fashion. Starting with separate optimization of the parameters describing each narrow component responsible for the more obvious discrete arcs, we minimized χ^2 over a rectangle around each apex. Table 1 lists the coordinates of the apexes of six of the most obvious reverse arcs. With five parameters for each Gaussian the number of parameters to fit grows quickly as components are added. To simplify we started with all components centered on the x-axis (ie $y_{oi} = 0$). With the position x_{oi} of a component fixed we explored the influence of σ_{xi} and σ_{yi}. For the arcs at large delays we found that σ_{xi} had to be quite narrow to agree with the observed arc thickness in delay, but that σ_{yi} could be substantially wider. As a result we did not optimize for the y-position or width, but set them all on the x axis with $\sigma_{yi} = 0.3$ mas. This left three parameters to be optimized for each component (amplitude, x-position and width). However, as discussed above the extent in q is governed by the x- position and width of the associated extended component, thus they too had to be adjusted.

Close inspection of the observed S_2 shows narrow parallel forward arcs crossing the reverse arcs. As can be seen from Figure 4 of CRSC, these are extensions of the reverse arc to positive f_t values which are reflected about the origin. Thus they show interference of a discrete component ($x_p < 0$) with components of the scattered brightness extended over a wide range, extending to x values more negative than x_p. This emphasizes that in

fact the entire set of arcs is caused by the mutual interference of all possible pairs of points in $b(x, y)$.

As noted above the observations show parallel forward arcs (for negative f_t), but they also include some that appear as fainter (whiter) stripes. Such fainter stripes come from a discrete minimum in $b(x, y)$, whereas the brighter arcs are from discrete maxima. We modelled this effect by putting dips into the brightness function, which we achieved by having two offset broad extended components with a minimum in b between them. These minima improved the fit slightly over a model without the minima. Thus in choosing how many and where to place new components, we were guided by the visual appearance of the observed S_2 in comparison with the model.

Table 2 gives a list of the parameters for the 9-component model for $b(x, y)$ (scaled into milliarcseconds). Components 1-6 are relatively narrow ($\sigma_x < 0.3$ mas) and components 7-9 are relatively wide. It is the interference of the narrow with the wide components that is responsible for the 6 most obvious discrete reverse arcs. Their position and width in Doppler frequency governs the range in x of the brightness function.

We optimized the model to minimize χ^2 with regard to the three variable parameters of the 9 components. The model can be seen in the upper panel of Figure 3, to be compared with the upper right panel of Figure 1. However, the value of χ^2 was about five times the number of points in the fit, indicating that the model is far from optimum even though it was a local minimum. The largest discrepancy was traced to the region near the f_t axis (from -1 to -2 cpm), in which the observed power level is elevated but the model is not. The higher level in the observations appears to be due to effects from broadband variation of the pulse strength (intrinsic pulse modulations or impulsive interference). Consequently, we estimated this extra power by averaging S_2 in (from -2 to -3 cpm) as a function of delay, and added it to the model.

This refinement caused little change in the best parameters but reduced the minimum χ^2 to about twice the number of data points. Visually, the model resembles the observations in the asymmetry versus f_t, the presence of 6 reverse arcs, the location of their apexes, and their width in delay (f_ν). Given the success of the fit from a visual perspective, we decided not to attempt a better fit by introducing extra components, since we would just be refining the model for a particular snapshot of the scattering function b. Further, since our method of fitting relies on the visual impression in choosing how many components and their initial parameters, the result is not unique.

The upper panel of Figure 3 shows the model secondary spectrum. It corresponds to the brightness model in Table 2 with one modification. In order to represent the "speckle" effect in a snapshot of the scattered brightness we multiplied the sum of Gaussians by a random function of x (uniform distribution), before computing the integral in equation (6). The effect is to cause a set of fine nearly parallel forward arcs, somewhat reminiscent of the observed fine structure in S_2. The model brightness is plotted logarithmically in the upper panel of Figure 4. Note the asymmetry and anisotropy in its distribution of discrete components along the axis parallel to $\mathbf{V}_{\rm iss}$.

The effect of rotating the brightness by an angle ϕ to the x-axis increases the magnitude of the curvature in p, q plane, as can be seen from equation (8). However, this could be compensated by a change in the screen distance parameter s. Thus we cannot determine both s and ϕ and leave our results displayed with $\phi = 0$.

We now consider what constraint can be placed on the y-extent of the brightness function ($b(x, y)$). When y_p and y_1 are non-zero, we obtain the a version of equation (8) in which y_p^2 is replaced by $y_p^2 - y_1^2$. Let the extended and point components be centered on the x-axis with widths σ_y and σ_{yp}, respectively. Then these ranges broaden the thickness of the reverse arc in delay (ie p is broadened by the larger of σ_y^2 and σ_{yp}^2. The widths of the reverse arcs in the upper right panel of Figure 1 are about $\pm 0.05 \mu$sec. With the scalings from equation (10), this constrains the rms y-widths to be less than about 0.44 mas. We set them (somewhat arbitrarily) to be 0.3 mas.

3.4. Discussion of the Model

Although the parameters we used gave us arc and subarc structures that resemble the particular PSR B1133+16 data, we do not imply that it is the only set nor is it the best set. We have produced one model for the brightness distribution that reproduces the visual form of the observations and

is optimized within a limited range of the parameters.

From this we conclude that the asymmetrical form of the observed secondary spectrum and the presence of narrow discrete reverse arcs can be successfully explained by an asymmetrical and anisotropic brightness function with a number of narrow discrete features. The constraint on the widths in θ_y is important since, with an θ_x-width of about ± 5 mas, it constrains the effective axial ratio of the scattered brightness function to be greater than about 10. However, an interesting feature of the model is that the individual features can be wider in θ_y than in θ_x; in other words they may be anisotropic in the orthogonal direction.

As shown by CRSC, an absence of power along the delay axis in the secondary spectrum is caused by anisotropic broadening, enhanced along the direction of the scintillation velocity. All of 12 of the secondary spectra plotted in Figure 2 show no power along the delay axis. Hence the same basic anisotropy in the scattering persisted over about 500 days, but the detailed form of the scattered brightness changed substantially over days and weeks.

3.5. Screen Simulation

CRSC used the simulation code of Coles et al. (1995) to simulate secondary spectra of waves scattered by a dispersive phase changing screen. In normal usage the method synthesizes one realization of a stationary random phase screen, which modulates a plane wave. The emerging complex field is then propagated a distance z to the observer, by transforming into wavenumber and multiplying by the appropriate (Fresnel) filter and back transforming to the spatial domain. The intensity is saved along a straight line track through the two-dimensional complex wave field. The result simulates a time series as an observer moves relative to a scattered wave field. A dynamic spectrum is a set of such time series, created as the radio frequency of the incident wave is incremented. The secondary spectrum is computed in the same way as for the data.

CRSC simulated the screen as a single two-dimensional realization of a stationary random process following a given wavenumber spectrum. They showed results for a Kolmogorov screen. When anisotropy was included, some results had multiple discrete forward and reverse arcs. However, the results differed from our observations of PSR B1133+16 in that the discrete arcs were considerably finer and distributed symmetrically in fringe rate (f_t). The addition of a linear gradient in the phase across the screen (i.e. a simple refraction) caused the secondary spectrum to be asymmetric in fringe rate. They showed that the phase gradient needed to be large enough to shift the scattered image by at least its own radius. This is a much larger gradient than is expected randomly for a medium with a Kolmogorov spectrum.

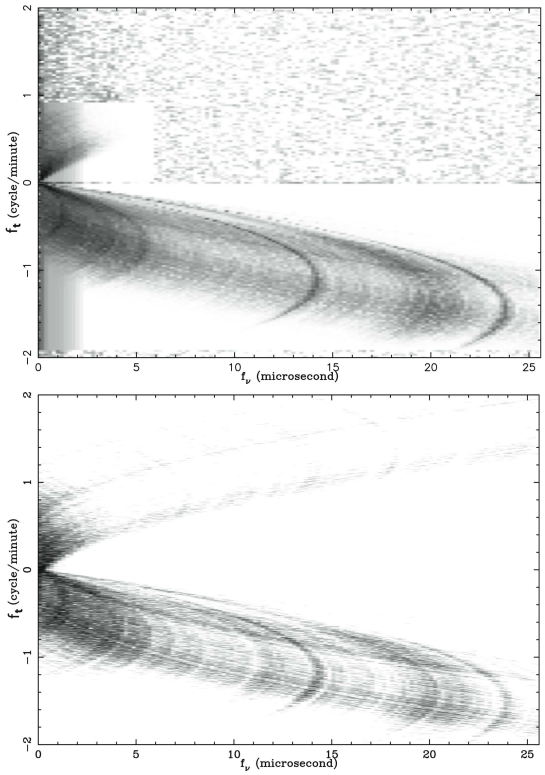

Fig. 3.— *Top*: Secondary spectrum computed from the brightness distribution of the upper panel of Figure 4, by a numerical integration of equation (6). Grey scale is logarithmic with dynamic range of 36 dB. The fit was done over the two rectangular regions shown; outside those regions the noise from the data is plotted. *Bottom*: Secondary spectrum from the screen simulation for the same day (see text) with dynamic range of 30 dB.

We modified the screen generation code to make the scattered brightness like that in our model

(i.e. the upper panel of Figure 4). This modification required an iteratative process, as follows. The field emerging from the phase screen at position $\mathbf{s}$ has unit amplitude and is phase modulated $F(\mathbf{s}) = \exp[j\phi(\mathbf{s})]$. Its two-dimensionsal Fourier transform $F^{\dagger}(\boldsymbol{\kappa})$ is the spectrum of the field versus wavenumber $\boldsymbol{\kappa}$, which maps simply to the scattered angle as $\boldsymbol{\kappa} = k\boldsymbol{\theta}$ with $k = 2\pi/\lambda$. Our goal is to find a screen phase $\phi(\mathbf{s})$, for which the squared magnitude $|F^{\dagger}|^2$ follows our model for the scattered brightness $B(\boldsymbol{\theta})$. We started by specifying the magnitude $F^{\dagger} = \sqrt{B(\boldsymbol{\theta}/k)}$ and assigned it random phase. Then back transformed to give $F(\mathbf{s})$, which had both amplitude and phase modulation. A revised $F(\mathbf{s})$ was obtained by normalizing each point to unit magnitude. That revised F was re-transformed and the resulting $F^{\dagger}$ was normalized to make its magnitude $\sqrt{B(\boldsymbol{\theta}/k)}$ and keep its phase. When this cycle was repeated the amplitude modulation in $F(\mathbf{s})$ is decreased. We iterated until the residual amplitude modulation no longer decreased ($\sim$ 100 cycles). The phase of this final $F(\mathbf{s})$ was then extracted as the screen phase for the normal simulation. This method is based on the concepts developed by Gerchberg and Saxton (1972). As in the normal simulation this screen phase was scaled proportional to radio wavelength, to represent the plasma dispersion.

The lower panel of Figure 3 gives the resulting secondary spectrum. It has the same basic features as the simple model in the upper panel, but shows more pronounced substructure in the form of fine arc modulations. The importance of this result is that the basic arc forms are unchanged by the inclusion of dispersion in the screen phase, whereas dispersion is not included in the physics of equation (6). A further result is that we have obtained a realization of the phase screen itself. This is then an estimate of the phase imposed by the ISM during the observations on our day 0, and we can ask what it tells about the density structure in the ISM.

3.6. Comparison with Reverse Arcs from PSR B0834+08

Hill, et al. (2005) reported how four discrete reverse arcs observed from PSR B0834+16 moved along the main forward parabola over 25 days. The Doppler frequency of the apex of each arc followed a linear track against time; furthermore the slopes of all four tracks were equal to the slope predicted by assuming that each reverse arc was scattered from a fixed structure in space scanned by the known pulsar proper motion. Their results suggest that the reverse arcs appearing on successive days are not unrelated, but are in fact due to the same physical structures.

We have attempted to test this idea with the reverse arcs observed on day 0 and 1 of our data (PSR B1133+16), which are 27 hours apart. For the 6 most obvious reverse arcs on day 0 we calculated the shift expected due to the pulsar proper motion in 27 hours and compared the new locations to those observed on day 1. The expected angular shift is $\delta\theta_x \sim \delta t V_{\rm pm}/D$, which we substitute into equation 10, and tabulate the f_t and f_ν positions before and after this proper motion shift (see Table 3). Comparing the shifted coordinates with those observed on day 1, we found some agreement. For example, the easily visible reverse arc no. 4 from day 0 should should move to f_t = -1.25 cpm and f_ν = 18.75 μs which is close to a prominent arc on day 1 (lower right panel of Figure 1). The comparison is complicated by the fact that day 1 shows a higher density of reverse arcs making it hard to recognize particular structures. We conclude that these data are not of sufficiently high signal to noise ratio to confirm or reject the hypothesis that the arc positions are simply shifted by the pulsar proper motion.

3.7. Relationship to W-S Inversion Algorithm

We now compare our model fitting with the method of Walker and Stinebring (2005) (WS) who estimate the scattered brightness function using an fitting algorithm to the dynamic spectrum. This has great appeal since it avoids the messy task of deciding what components of the secondary spectrum to include in a model fit. Their method represents the full electric field as a sum of "scattered waves", which are successively identified and subtracted in order to match the observed primary dynamic spectrum to the model. It is somewhat analogous to the CLEAN algorithm in image reconstruction.

WS consider the scattered electric field $U(\nu, t)$ at frequency ν and time t as a sum of basis functions $\exp[i2\pi(\nu f_t + f_\nu t)]$, which they call scattered waves, though the formulation is not derived from

scattering theory. We note that ν and t are relative to the center of the observing band and integration time and that WS use the symbols τ for f_ν and ω for f_t.

The dynamic spectrum $S(\nu, t)$ is then modelled by $|U(\nu, t)|^2$ and WS designed a procedure to estimate the phasor $(\tilde{U}(f_\nu, f_t))$ for each scattered wave to best match the model with the observed dynamic spectrum. The results are given as both amplitude and phase for each differential delay f_ν and Doppler f_t. They applied the method and displayed the amplitudes for a particular 327 MHz observation in the sequence from PSR B0834+06 (Hill et al., 2005), in which there were several well-defined reverse arclets. They discuss possible applications of the method but do not relate the results to the scatttered brightness $B(\theta_x, \theta_y)$.

However, Asplund et al. (2004) used these same results and mapped them to the scatttered brightness by assuming that each component $\tilde{U}(f_\nu, f_t)$ was the result of interference between an undeviated (reference) wave and a wave scattered at angle (θ_x, θ_y). This assumption is valid under conditions of weak scattering, as shown by CRSC, but it does not seem justified for the 327 MHz observations of PSR B0834+06. As WS note, the effective reference wave in their algorithm starts out as undeviated, but is modified as each scattered wave component is identified. Nevertheless the summing of the "scattered waves" does include the mutual interference between the components of the basis functions as well as their interference with the reference component.

One can show that the secondary spectrum is the square of the auto-correlation of $\tilde{U}(f_\nu, f_t)$, as follows:

$$S_2(f_\nu, f_t) = |\sum_{F_\nu}\sum_{F_t} \tilde{U}(F_\nu, F_t)\,\tilde{U}*(F_\nu + f_\nu, F_t + f_t)|^2 \quad (13)$$

Nevertheless, it seems that more work is needed on the theoretical basis of the algorithm to consider the circumstances under which the weak scintillation mapping into the angle domain is properly justified.

While the method we have used is cumbersome to implement, it is more straightforward in that our computed model directly sums the waves in the domain of (θ_x, θ_y) including their mutual interference.

4. The Density structure in the Interstellar Plasma

Most interpretations of radio scintillation have been formulated as constraints on the wavenumber spectrum of the plasma density. The Kolmogorov spectrum has become a default model, even though several observations point to more fluctuation power on wavelengths longer than the size of the typical radio scattering disc (a few AU).

The general concept proposed to explain the discrete reversed arcs is that substructure in the scattered brightness b, analogous to speckle in a scattered image, causes substructure in the secondary spectrum, that takes on a form of points lying on intersecting reverse and forward parabolic arcs, traced by equation (8) and its reflection in the origin, with intensity at each point governed by the product of the brightness of the two interfering components. The plots in Figure 4 are estimates of a single realization of the scattered brightness with a particular sub-structure characteristic of the observing conditions. We now consider what these images tell us about the density structure in the interstellar plasma.

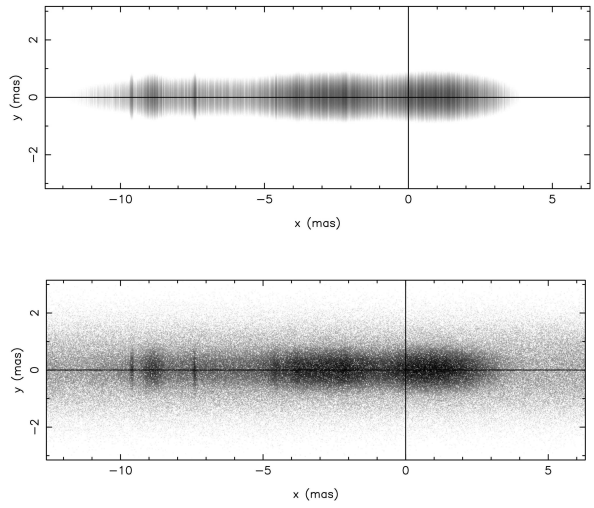

Fig. 4.— *Top*: Logarithmic plot of the model brightness distribution obtained by fitting to observation on day 0 in Figure 1 (dynamic range 50 dB). *Bottom*: brightness distribution obtained from the full screen simulation (see text).

The first point is that the scattered image is

highly elongated with an axial ratio of 10:1 or more. Further, the axis of elongation is roughly parallel to the proper motion direction of the pulsar (within, say, $\pm 20^\circ$). This means that the spatial density structures are elongated in a direction roughly perpendicular to this direction.

The second point is that the images are not centered on the origin. We see two possible explanations: either refraction by a large scale transverse gradient in the column density of electrons; or highly localized scattering caused by a region that is centered to one side of the line towards the pulsar.

Refraction seems likely since similar refraction has been invoked to explain the persistent drifting in frequency of scintillation features in the dynamic spectra of some pulsars (e.g. Shishov, 1974; Hewish, Wolszczan and Graham, 1985; Gupta, Rickett and Lyne, 1994). The basic idea is that a refracting region deflects the scattered (and unscattered) waves which causes a lateral shift in the scintillation pattern. Since in a plasma the angle of refraction is strongly dependent on the observing frequency, the frequency for a given maximum of intensity will drift in time. Such a drift will be seen as an asymmetry versus Doppler frequency in the power distribution of the secondary spectrum, this effect was confirmed by simulations reported by CRSC.

The alternative explanation is that there are highly localized regions of very irregular (turbulent?) plasma, that can deflect (ie scatter or refract) the radio waves into our line of sight. This implies that thay must be small enough to subtend an angle at the observer smaller than their maximum angle of deflection. The angles of arrival of these waves will be determined by how far the enhanced turbulence is from the direct line of sight and they will not depend systematically on frequency.

A third point about the scattered images is that they are "blotchy", but the blotches have a lower filling factor than would be expected for the usual speckle in an angular spectrum. (see the simulations shown by CRSC, in which there is a multitude of reverse arcs due to speckle with a high filling factor from a Kolmogorov medium). We conclude that the blotchy nature of our scattered image is not compatible with a uniform Kolmogorov random medium. Our results do not, on their own, allow us to determine the nature of the medium. However, the fascinating measurements by Hill et al. (2005) for pulsar PSR B0834+06 provide an important constraint. They found that the frequency-scaling of the positions of the reverse arcs was not compatible with frequency dependent refraction and implies the alternative of highly localized regions of enhanced scattering as the cause of each reverse arc. Under this scenario the regions have a linear size given by their apparent angular size times the scattering distance – $D(1-s) \sim 140$ pc. With angular extents of 0.1-1 mas their maximum implied linear sizes are 0.014-0.14 AU.

Considering that the discrete reverse arcs were only prominent in some of the observations (ie days 0-31 and 288), the regions of localized enhanced scattering are irregularly distributed in the ionized ISM. In 31 days the pulsar moves about 10 AU transverse to the line of sight. Thus the persistence of the reverse arcs through 31 days suggests that the localized regions of enhanced scattering are clumped over about 10 AU.

If localized scattering regions are indeed responsible for the discrete reverse arcs, the next question is what are these regions physically. However, this is beyond the reach of our present investigation, and we refer interested readers to Rickett, Lyne and Gupta (1997) and the proceedings of the workshop on "Small Ionized and Neutral Structure in the ISM", held in Socorro May 2006, particularly the papers by Stinebring and Rickett.

5. Conclusion

The ISS of pulsar B1133+16 showed pronounced changes in the character of its secondary spectra in 12 days of observation spread over 15 months. While these data which were centered at 408 MHz were recorded over 20 years ago, they often show the parabolic arc phenomenon that was discovered quire recently by Stinebring et al. (2001). However, the basic parabolic arc varied substantially in its extent and shape. Discrete reverse arcs were visible for about two months early in the sequence and then again after about nine months. There was a two month interval when the arc was barely detectable, corresponding to when the primary dynamic spectra had a very wide decorrelation bandwidth.

We concentrated our analysis on two days with clearly visible discrete reverse arcs, which were fortuitously sampled rapidly enough to resolve them in Doppler frequency. Using the theory of CRSC, which ignores dispersion, we modelled these features and hence were able to estimate the scattered brightness distribution. We tested the applicability of the theory, by simulating and electromagnetic wave propagation code that includes dispersion, and found that the reverse arcs are not altered substantially by including dispersion.

Our estimate of the scattered brightness function is highly eleongated with an axial ratio of more than 10:1. It is asymmetrical about the origin and has a small number of discrete maxima. These properties are not consistent with expectations from a scattering region that behaves as a statistically homogeneous random medium with a Kolmogorov spectrum. When combined witth the conclusions from Hill et al. (2005), our results suggest that there are highly localized discrete scattering regions which subtend 0.1-1 mas, but can scatter (or refract) the radiation by angles that are five or more times larger. The asymmetry in the scattered image may well be caused by the chance configuration of these regions.

We thank Andrew Lyne for completing the series of observations at Jodrell Bank in 1984-85 and we thank Yashwant Gupta for work on the original data reduction. We thank the National Science Foundation for support under grants AST 9988398 and AST 0507713.

REFERENCES

Asplund, C. T., Berwick, D. E., Stinebring, D. R. & Walker, M. A., 2004, "Milliarcsecond Images of the Ionized ISM From Pulsar Scintillation", American Astronomical Society Meeting Abstracts, 205 ,13912

Brisken, W. F., Benson, J. M., Goss, W. M. & Thorsett, S. E. 2002. ApJ, 571, 906.

Coles, W.A., Filice, R.G., Frehlich, R.G., and Yadlowsky, 1995, Applied Optics, 34, 2089

Cordes, J. M. and Rickett, B. J. 1998, ApJ, 507, 846

Cordes, J. M., Rickett, B. J., Stinebring, D. R., & Coles, W. A. 2006, ApJ, 637, 346

Gerchberg, R. W., & Saxton, W. O. 1972, Optik, 35, 237

Gupta, Y., Rickett, B. J., & Lyne, A. G. 1994, MNRAS, 269, 1035

Hewish, A., Wolszczan, A. & Graham, D.A. 1985, MNRAS, 213, 167

Hill, A. S., Stinebring, D. R., Barnor, H. A., Berwick, D. E., & Webber, A. B. 2003, ApJ, 599, 457

Hill, A. S.; Stinebring, D. R.; Asplund, C. T.; Berwick, D. E.; Everett, W. B.; Hinkel, N. R. 2005, ApJ, 619L, 171

Putney, M. L. & Stinebring, D.R. 2006, "Multiple Scintillation Arcs in Six Pulsars," and then the ChJAA reference (w/ editors, etc.)

Rickett, B. J., Lyne, A. G., & Gupta, Y. 1997, MNRAS, 287, 739

Shishov, V.I. 1974, *Sov. Astron. AJ* , 17, 598

Stinebring, D. R., McLaughlin, M. A., Cordes, J. M., Becker, K. M., Espinoza Goodman, J. E., Kramer, M. A., Sheckard, J. L., & Smith, C. T. 2001, ApJ, 549, L97

Walker, M. A., Melrose, D. B., Stinebring, D. R. & Zhang, C. M. 2004, MNRAS, 354, 43

Walker, M. A. & Stinebring, D. R. 2005, MNRAS, 362, 1279

This 2-column preprint was prepared with the AAS LaTeX macros v5.2.

Subarc Coordinates (Observation vs. Model)

	Observation		Model	
Subarc #	f_t (cpm)	f_ν (μs)	f_t (cpm)	f_ν (μs)
1	-0.31	1.2	-0.32	1.22
2	-0.58	3.8	-0.56	3.82
3	-0.69	5.4	-0.67	5.43
4	-1.09	14.0	-1.10	14.22
5	-1.31	20.0	-1.30	20.36
6	-1.44	23.6	-1.41	23.86

Table 1: The coordinates of the observed individual subarcs (day 0, Figure 1: *Top Right*) and the modeled subarcs (Figure 3: *Top*).

Parameters for Model Brightness Distribution

Component (i)	(A_i)	(x_{oi})	(σ_{xi})	(y_{oi})	(σ_{yi})
1	0.418	-2.18	0.138	0	0.32
2	0.273	-3.85	0.104	0	0.32
3	0.127	-4.59	0.126	0	0.32
4	0.327	-7.42	0.041	0	0.32
5	0.2	-8.88	0.261	0	0.32
6	0.236	-9.62	0.038	0	0.32
7	1.0	0.82	1.04	0	0.32
8	0.545	-2.68	1.418	0	0.32
9	0.027	-7.25	2.111	0	0.32

Table 2: Components of the brightness distribution defined by equation 11 where the angular units are mas. These values were used in Figure 3 to model the observations of day 0

Subarc Coordinates (Day 0 vs. Proper Motion)

	Before		After	
Subarc #	f_t (cpm)	f_ν (μs)	f_t (cpm)	f_ν (μs)
1	-0.32	1.22	-0.48	2.78
2	-0.56	3.82	-0.73	6.32
3	-0.67	5.43	-0.83	8.35
4	-1.10	14.22	-1.25	18.75
5	-1.30	20.36	-1.46	25.72
6	-1.41	23.86	-1.57	29.63

Table 3: The coordinates of the individual subarcs before (day 0, Figure 1: *Top Right*) and after the shift due to the pulsar proper motion.